CHEMISTRY

Single-molecule photocatalytic dynamics at individual defects in two-dimensional layered materials

Teng-Xiang Huang[1†], Bin Dong[1†], Seth L. Filbrun[1], Aisha Ahmad Okmi[2], Xiaodong Cheng[1,3], Meek Yang[1], Nourhan Mansour[1], Sidong Lei[2]*, Ning Fang[1,3]*

Copyright © 2021 The Authors, some rights reserved; exclusive licensee American Association for the Advancement of Science. No claim to original U.S. Government Works. Distributed under a Creative Commons Attribution NonCommercial License 4.0 (CC BY-NC).

The insightful comprehension of in situ catalytic dynamics at individual structural defects of two-dimensional (2D) layered material, which is crucial for the design of high-performance catalysts via defect engineering, is still missing. Here, we resolved single-molecule trajectories resulted from photocatalytic activities at individual structural features (i.e., basal plane, edge, wrinkle, and vacancy) in 2D layered indium selenide (InSe) in situ to quantitatively reveal heterogeneous photocatalytic dynamics and surface diffusion behaviors. The highest catalytic activity was found at vacancy in a four-layer InSe, up to ~30× higher than that on the basal plane. Moreover, lower adsorption strength of reactant and slower dissociation/diffusion rates of product were found at more photocatalytic active defects. These distinct dynamic properties are determined by lattice structures/electronic energy levels of defects and layer thickness of supported InSe. Our findings shed light on the fundamental understanding of photocatalysis at defects and guide the rational defect engineering.

INTRODUCTION

Defect-rich two-dimensional (2D) layered materials have been the most promising candidate catalysts that can replace noble metals in catalysis (*1*, *2*). Although defects are small, at nanometer to the atomic level, they play a notable role in catalysis as the catalytically active sites in 2D layered materials (*3*, *4*). Because defects can induce lattice reconstruction, create unsaturated coordination sites, alter local charge carrier density, and change electronic band structures, they introduce unique chemical and electronic properties and dictate the catalytic behaviors and reaction mechanisms of 2D layered materials (*4*, *5*). Therefore, defect engineering, such as vacancy fabrication, surface doping, and strain modulation, has emerged as a key approach to activate the inert basal plane and improves the performance of 2D layered material-based catalysts (*4*).

Spatially resolved characterizations of individual defects enable one to unveil their inhomogeneities in intrinsic physicochemical properties and catalyzed reaction dynamics, which are crucial for the design of high-performance 2D layered material catalysts via defect engineering. Up to now, most efforts have been devoted to investigating the physicochemical properties of defects in 2D layered materials (*6*–*9*). For example, annular dark-field scanning transmission electron microscopy (*6*) and scanning tunneling spectroscopy (*7*) were used to characterize the lattice structure and electronic properties of defects at atomic scale, respectively, under ultrahigh vacuum and even ultralow temperature. Tip-enhanced spectroscopies, such as tip-enhanced Raman spectroscopy (*8*) and nanoscale infrared spectroscopy (*9*), can reveal the structural and electronic properties of defects at nanometer scale in realistic conditions. However, the fundamental understanding of in situ catalytic dynamics at individual defects, which ultimately guides the defect engineering of 2D layered material catalysts, is still missing. Dynamic processes in a chemical reaction catalyzed on the catalyst surface involve the adsorption, activation, and chemical conversion of the reactant and the dissociation (including the diffusion and desorption) of the final product. All these dynamic steps contribute to the turnover frequency of a catalytic reaction. The structures, chemical composition, and electronic properties of active sites such as defects in 2D layered materials can alter these dynamic steps and further determine their catalytic properties (*10*). Unveiling individual reaction dynamic steps at defects will help establish the structure-dynamic property relationship and, in turn, guide the rational defect engineering for 2D layered material-based catalysts.

Single-molecule fluorescence imaging, with the capability of counting single turnover reaction events and nanometer spatial resolution (<20 nm), has been used to study the heterogeneities in catalysis at active sites in single solid catalysts, such as metal/semiconductor particles (*11*, *12*), crystals (*13*), and porous materials (*14*–*16*). Here, we used single-molecule fluorescence imaging to spatially resolve the in situ photocatalytic dynamics at individual structural features (i.e., basal plane, edge, wrinkle, and vacancy) in 2D layered indium selenide (InSe). We deconvoluted the individual dynamic steps in a photocatalytic reaction at single-molecule level and quantitatively measured reactant adsorption strength, chemical conversion rate, product dissociation rate, and surface diffusion processes at individual defects. Moreover, our experimental results unveiled very distinct layer thickness effects on photocatalytic dynamic processes at individual defects. These findings are essential for improving the performance of 2D layered material catalysts via rational defect engineering.

RESULTS

Heterogeneous photocatalytic activities at individual defects

We first transferred mechanically exfoliated few-layered InSe onto a quartz slide. Next, a microflow chamber was assembled with the sample-loaded quartz slide and a coverslip using double-sided tape (fig. S1). A continuous flow of the reactant solution was supplied over the InSe flakes. When InSe flakes are illuminated with ultraviolet

[1]Department of Chemistry, Georgia State University, Atlanta, GA 30303, USA. [2]Department of Physics and Astronomy, Georgia State University, Atlanta, GA 30303, USA. [3]State Key Laboratory of Physical Chemistry of Solid Surfaces, Innovation Laboratory for Sciences and Technologies of Energy Materials of Fujian Province (IKKEM), College of Chemistry and Chemical Engineering, Xiamen University, Xiamen 361005, Fujian, China.
*Corresponding author. Email: nfang@xmu.edu.cn (N.F.); slei@gsu.edu (S.L.)
†These authors contributed equally to this work.

light at 365 nm, photo-induced electrons (e^-) and holes (h^+) are generated and can oxidize a very weakly fluorescent reactant molecule [3-aminophenyl fluorescein (APF)] to the highly fluorescent product molecule fluorescein (Fig. 1A and fig. S2A) by either the ·OH pathway (*17*) or the direct oxidation pathway (see section S2) (*18*). The product molecule fluorescein was excited by a 488-nm laser in a total internal reflection (TIR) configuration. The fluorescence signals were collected by a high numerical aperture (NA, 1.2) water immersion objective and imaged on a highly sensitive electron multiplying charge-coupled device camera (fig. S1). Photocatalytic events that occurred on InSe surface were imaged (Fig. 1B), and the stochastic on-off fluorescence signals with one-step intensity change indicated a single photocatalytic event (Fig. 1C). Multiple photocatalytic events that happened within the same on-off period (fig. S4) made up a very low population in our imaging experiments and were excluded from the quantitative analysis of reaction kinetics. The center positions of product molecules were super-localized with nanometer-scale precision through point spread function fitting (fig. S5) to produce the maps of locations where the APF oxidation reaction happened (Fig. 1D).

As shown in Fig. 1D, the number of catalytic events (shown in color) at different structural features is clearly distinguishable, indicating the photocatalytic activity heterogeneity over 2D layered InSe. The basal plane and edge commonly exist in the mechanically exfoliated InSe flakes, while wrinkle and vacancy are inevitably introduced by the exfoliation and transferring (*19*, *20*). Section S4 shows the detailed identification of defects. Edges and wrinkles are visible optically in bright-field images. A control experiment with argon plasma, which can produce surface vacancies (*21*), helps identify vacancies in single-molecule imaging. From the localization mapping results (Fig. 1D), we directly observed higher photocatalytic activities (brighter intensity means more catalytic events) at the edge, wrinkle, and vacancy in comparison to that on the basal plane. More localization mapping results of InSe flakes are provided in fig. S10. Counting the single turnover events at subregions (see section S5 for more details) of all structural features allows us to quantify the specific catalytic turnover rate, ν_T, as the number of catalytic events over time and area of subregions. Fitting the distribution of ν_T at subregions of all structural features (Fig. 1E), we determined averaged specific catalytic turnover rates ($<\nu_T>$, where < > denotes

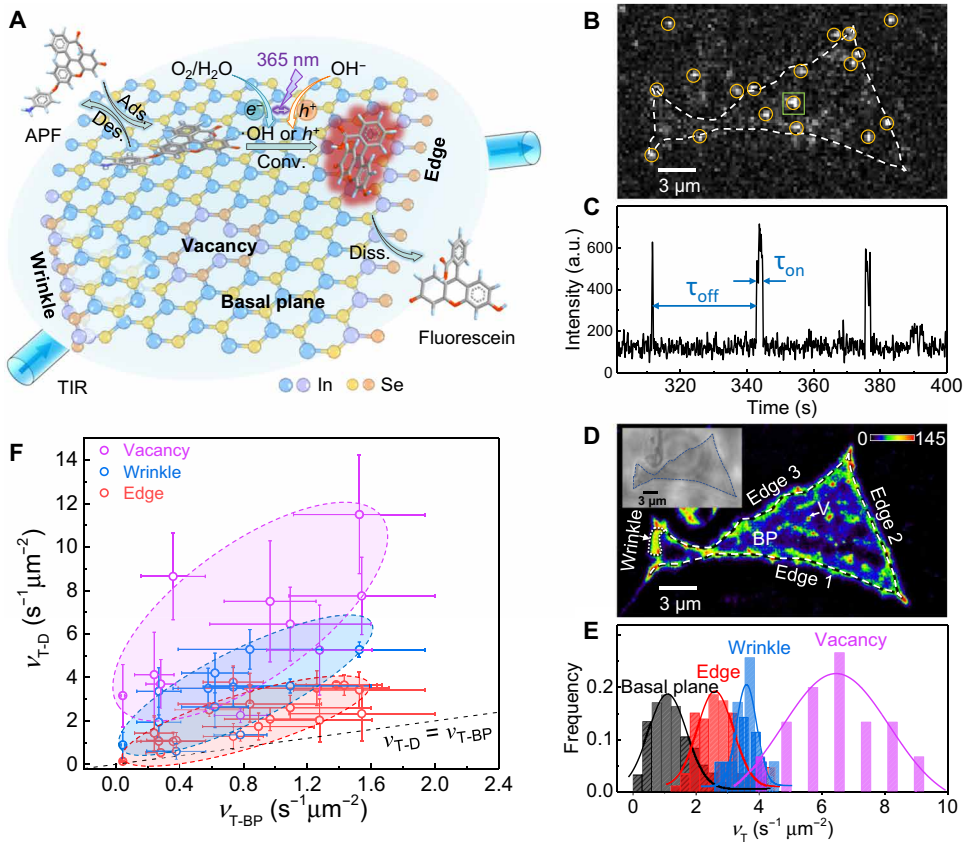

Fig. 1. Single-molecule fluorescence imaging of heterogeneous photocatalytic activities on 2D layered InSe flakes. (**A**) Schematic of experiment setup. (**B**) Typical single-frame image of products fluorescein (highlighted by yellow circles) produced on InSe. Dashed line shows the contour of a four-layer InSe flake. (**C**) Segment of a typical fluorescence intensity trajectory from 400 nm by 400 nm area on the basal plane (BP) marked by the green square in (B). a.u., arbitrary units. (**D**) Localization mapping of photocatalytic activities on InSe flake for a data collection period of ~23 min. Dashed lines denote edges. Dotted lines denote a folding layer. The edge of this region marked by an arrow denotes a wrinkle. White arrow denotes a vacancy (V). The color bar denotes the number of products detected over an area of 24 nm by 24 nm. Inset: The optical bright-field image. (**E**) Histogram distributions of turnover rates (ν_T) at subregions of these four structural features. (**F**) Statistic plot of $<\nu_T>$ at various defects ($\nu_{T\text{-}D}$) versus $<\nu_T>$ on the basal plane ($\nu_{T\text{-}BP}$) from 20 InSe flakes. The *x* and *y* error bars are the SDs in Gaussian fitting the distribution of $\nu_{T\text{-}BP}$ and $\nu_{T\text{-}D}$, respectively. The colored ellipses are guides for the eye.

averaging) of 1.1 ± 0.6, 2.6 ± 0.6, 3.6 ± 0.3, and 6.5 ± 2 s^{-1} μm^{-2} at the basal plane, edge, wrinkle, and vacancy, respectively. This result shows that vacancy has the highest photocatalytic activity. We also observed a similar trend in another example (fig. S11). Figure 1F shows the results from 20 InSe flakes and compares $<v_T>$ on the basal plane ($v_{T\text{-}BP}$) and $<v_T>$ at defects ($v_{T\text{-}D}$). We find out that all defects have higher photocatalytic activity than the basal plane, and photocatalytic activity of defects decreases in the order of vacancy, wrinkle, and edge.

In situ quantification of photocatalytic kinetics at individual defects

Deconvoluting the dynamic step in catalytic reaction is critical for understanding the detailed kinetic processes and optimizing the photocatalytic properties accordingly. Single-molecule imaging enables the monitoring of individual catalytic events; thus, the quantification of kinetics (i.e., adsorption equilibrium, chemical conversion of the reactant, and the dissociation of the product) can be realized through analyzing these events with turnover resolution. In the fluorescence intensity trajectory (Fig. 1C), τ_{off} is the waiting time before each product molecule fluorescein formation (fig. S12A). Once the product molecule fluorescein dissociates from the catalyst surface, it quickly diffuses out of the evanescent field depth [~200 nm (*22*) from interface] in TIR fluorescence microscopy under a continuous flow of reactant solution and can no longer be detected. Therefore, τ_{on} can be attributed to the waiting time for the fluorescein dissociation from the InSe (fig. S12B), which is much shorter than the photobleaching lifetime of fluorescein [tens of seconds (*23*, *24*)]. Resolving $<\tau_{off}>^{-1}$ and $<\tau_{on}>^{-1}$ enables us to determine the reaction rate ($v_{APF} = <\tau_{off}>^{-1}$/area) of the photocatalysis of reactant APF and dissociation rate ($v_d = <\tau_{on}>^{-1}$) of product fluorescein (see details in sections S5 and S6).

Figure 2A (top) shows the reaction kinetic data at different structural features of the same InSe flake in Fig. 1B. At all types of structural features, the photocatalytic reaction kinetic data follow the Langmuir-Hinshelwood (LH) kinetic model (*25*–*29*) where the reaction rate increases initially at low reactant concentrations and saturates at high reactant concentrations eventually. The distinct kinetic data (Fig. 2B) suggest the inhomogeneity of photocatalytic reaction kinetics at different structural features. In the LH kinetic model, the reaction mechanism can be quantitatively described as $\upsilon_{APF} = \frac{k_{eff} K_{APF}[APF]}{1 + K_{APF}[APF]}$, where k_{eff} is the chemical conversion rate constant and K_{APF} (i.e., k_{ads}/k_{des}) is the adsorption equilibrium constant (fig. S12A). By fitting the reaction kinetic data (Fig. 2A) with the LH model, k_{eff} and K_{APF} at different structural features were

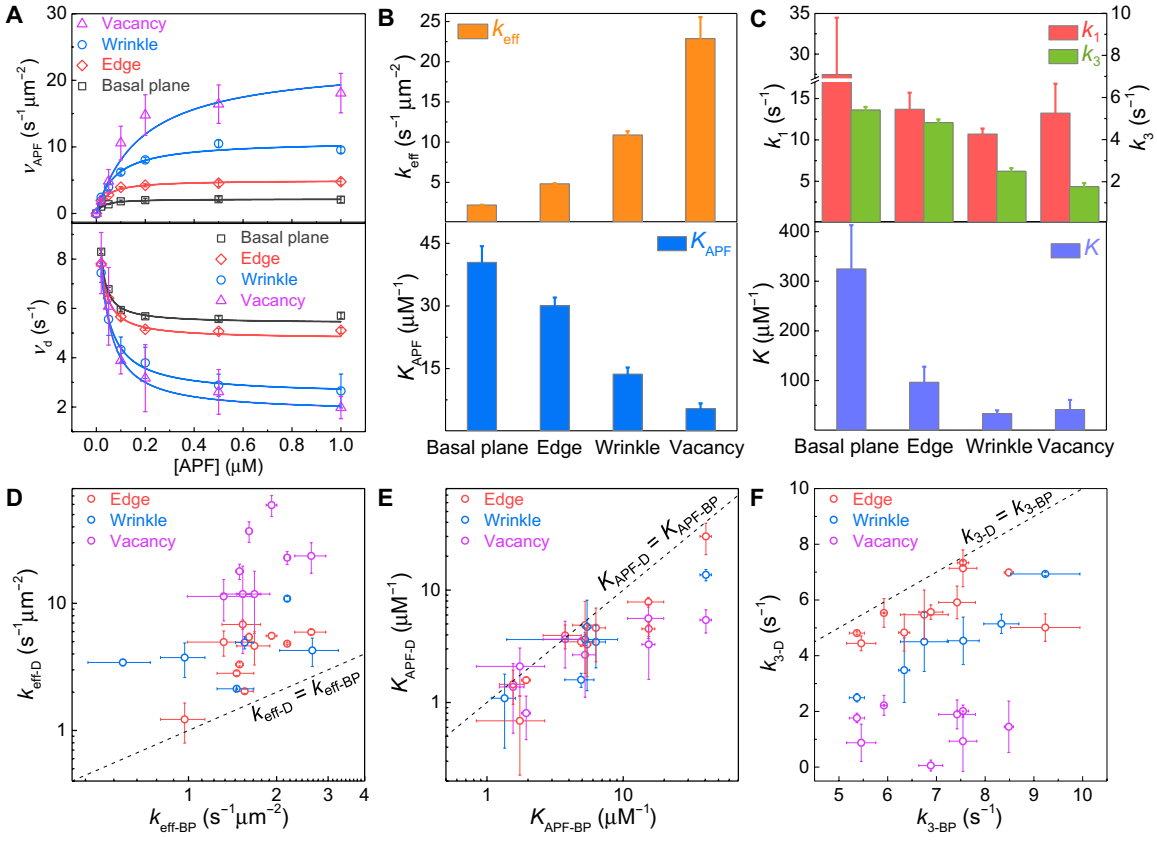

Fig. 2. Photocatalytic reaction kinetics at different structural features of InSe in Fig. 1. (**A**) APF concentration dependence of APF reaction rate (v_{APF}) (top) and fluorescein dissociation rate (v_d) (bottom). The error bars are the SDs in Gaussian fitting the distribution of catalytic reaction rates from many subregions (basal plane > 250, edge > 80, wrinkle > 30, and vacancy > 10). (**B** and **C**) Reaction rate constant k_{eff} [(B), top], adsorption equilibrium constant of APF K_{APF} [(B), bottom], direct and indirect desorption rate constants of fluorescein k_1 and k_3 [(C), top], and K [$K = k_2/(k_{-2} + k_3)$] [(C), bottom] at different structural features of InSe. The error bars were determined from fitting the kinetic data. (**D** to **F**) Comparison of k_{eff} (D), K_{APF} (E), and k_3 (F) on the basal plane ($k_{eff\text{-}BP}$, $K_{APF\text{-}BP}$) and at defects ($k_{eff\text{-}D}$, $K_{APF\text{-}D}$) in same InSe flakes ($n = 12$). The error bars were determined from fitting the kinetic data.

uncovered (Fig. 2B). In this specific sample (Fig. 1), the basal plane has the least k_{eff} of 2.2 ± 0.1 s^{-1} μm^{-2}. The three defects, i.e., edge, wrinkle, and vacancy, have k_{eff} that are 2.2, 5.0, and 10.5 times larger than that on the basal plane, respectively. However, K_{APF} shows the opposite trend.

Figure 2 (D and E) shows the statistic results of k_{eff} and K_{APF} at defects ($k_{eff\text{-}D}$, $K_{APF\text{-}D}$) versus those on the basal plane ($k_{eff\text{-}BP}$, $K_{APF\text{-}BP}$) in same InSe flakes (n = 12 individual InSe flakes). For the same InSe flake, vacancies, wrinkles, and edges show up to ~30×, ~6×, and ~4× higher photocatalytic reaction rate constant but up to ~7×, ~3×, and ~3× smaller absorption equilibrium constant, correspondingly, when compared with the basal plane. Defects such as edge, vacancy, and wrinkle can bend the intrinsic energy band and induce the local built-in electrical field. Driven by this field, the photogenerated electrons and holes rapidly accumulate on or escape from these defect sites, thereby affecting the charge separation processes. We attribute the distinct reaction kinetics at different InSe structural features to their different efficiencies in photogeneration and separation of electron-hole pairs. At wrinkles, both the tensile and compressive strain (fig. S14B) (*30*) can be created and form type I and type II electronic band alignments with nearby pristine InSe, respectively (section S7) (*31*–*34*). The former type can increase the total amount of photogenerated charge carriers (fig. S14C), whereas the latter type can enhance the charge separation efficiency (fig. S14D), which explains the higher photocatalytic activities at the wrinkle as compared to that on the basal plane. At the unsaturated defects (i.e., edge and vacancy), In—O bonds can be easily formed upon oxidation when exposed to air/water (*35*–*37*) and form a type II band alignment (fig. S14E) between the oxidized defects and the nearby pristine InSe (*34*, *38*). Thus, higher charge separation efficiency is induced, and the photocatalytic activity is enhanced at these unsaturated defects as compared to that on the basal plane. Nevertheless, other factors, including different photon absorption efficiency (*33*) and effective mass of the electron and hole (*39*) at different structural features, may also cause different photocatalytic activities. On the other hand, an aromatic molecule such as APF tends to lay down flatly on the basal plane to obtain the strongest van der Waals (vdW) attraction force (*40*) thus has the largest K_{APF}. In contrast, the steric effect induced by lattice reconstruction in defects (i.e., edge, wrinkle, and vacancy) would hinder the preferably flat adsorption configuration (*40*), weaken the vdW attraction between APF and defects, and reduce K_{APF}. In our single-molecule imaging experiments (pH 7.4), APF is negatively charged [benzoic acid [pK_a (where K_a is the acid dissociation constant), ~4.2] and benzenamine (pK_a, ~4.6)]. Therefore, the distinct electronic environment at defects induced by the local built-in electrical field should also affect the adsorption of APF molecules through the electrostatic interaction. These factors are combined to take effect, and they cannot be verified separately in this experiment.

On the other hand, the dissociation kinetics of fluorescein at different structural features (Fig. 2A, bottom) follow the same trend where the dissociation rate is initially fast but decreases at higher [APF] and eventually approaches a saturation level. The dissociation kinetic data indicate more complex processes than a simple direct dissociation of fluorescein, which should be independent of reactant concentration. For the fluorescein dissociation during the τ_{on} period, previous works (*25*, *26*) show that two possible parallel pathways (fig. S12B) can exist: a direct dissociation pathway (step 1) and a reactant-assisted pathway involving the participation of reactant (steps 2 and 3). Therefore, the kinetics of fluorescein dissociation can be described by the equation of $\nu_d = \frac{k_3 K[\mathrm{APF}]+k_1}{1+K[\mathrm{APF}]}$, where $K = \frac{k_2}{k_{-2}+k_3}$ (*26*). k_1 and k_3 represent the dissociation rate constant of the direct and reactant-assisted dissociation pathways and dominate at the low and high [APF], respectively. k_2 and k_{-2} are the adsorption and desorption rate constants of APF in the reactant-assisted dissociation pathway. Fitting the dissociation kinetic data (Fig. 2A, bottom, solid line) gives corresponding kinetic parameters as shown in Fig. 2C.

We found that the direct dissociation rate constants k_1 are much larger than the reactant-assisted dissociation rate constants k_3 at all structural features (Fig. 2C, top). This explains why the total dissociation rate decreases with the increase of APF concentrations, where the reactant-assisted dissociation pathway (slower dissociation rate k_3) gradually dominates (Fig. 2A, bottom). Because high concentration of reactant is used in the real application of catalysts, k_3 can reflect the dissociation rate of the product molecule. In this specific sample (Fig. 1), k_3 (Fig. 2C, top) at the basal plane (5.4 ± 0.2 s^{-1}), edge (4.8 ± 0.2 s^{-1}), wrinkle (2.5 ± 0.1 s^{-1}), and vacancy (1.8 ± 0.2 s^{-1}) are in descending order. Figure 2F shows the statistic results of k_s at defects ($k_{eff\text{-}D}$, $K_{APF\text{-}D}$) versus those on the basal plane ($k_{eff\text{-}BP}$, $K_{APF\text{-}BP}$) in same InSe flakes (n = 12 individual InSe flakes). For the same InSe flake, vacancies, wrinkles, and edges show up to ~26×, ~2.2×, and ~1.8× smaller dissociation rate constants, correspondingly, when compared with the basal plane. Furthermore, a larger K on the basal plane than that in defects (Fig. 2C, bottom) suggests that the dissociation on the basal plane is more sensitive to the [APF], and the population of molecules following the indirect dissociation pathway is larger on the basal plane than that at defects under the same reactant concentration.

Layer-dependent photocatalytic kinetics at individual defects

The thickness of pristine 2D layered materials has notable impact on their catalytic properties (*41*). However, the influence of layer thickness on the catalysis at individual defects is unknown. Figure 3 shows the layer-dependent photocatalytic kinetic results at the basal plane, edge, and vacancy. See section S8 for details on the identification of layer number. As shown in Fig. 3A, basal plane and vacancy sites are those at the top exposed layer, and different layers of the few-layered InSe always share the same edge in the 2D view. Because wrinkle is randomly formed during the mechanical exfoliation and transfer processes, it is difficult to consistently find wrinkles in all InSe flakes. Therefore, we excluded the data of wrinkles in the following discussion. Because the interlayer spacing of InSe is only 2 to 3 Å (*42*), no reaction can happen in the internal layers. In all samples studied, vacancy is the most active (k_{eff}), whereas the basal plane is the least active (Fig. 3B). k_{eff} does not change significantly when the thickness of 2D InSe is larger than eight layers, whose physicochemical property becomes similar to that of the bulk InSe. The highest k_{eff} is found at a thickness of three to four layers for all structural features, which can be explained as the balanced result of two factors, i.e., electronic band structure and photon absorption efficiency. First, InSe has a direct bandgap structure when the layer number is more than six but becomes an indirect bandgap semiconductor when the layer number decreases down to five (*43*, *44*). The indirect bandgap semiconductor has a lower possibility of recombination of photogenerated electrons and holes than the direct bandgap semiconductor. Thus, the separated electrons and holes in indirect

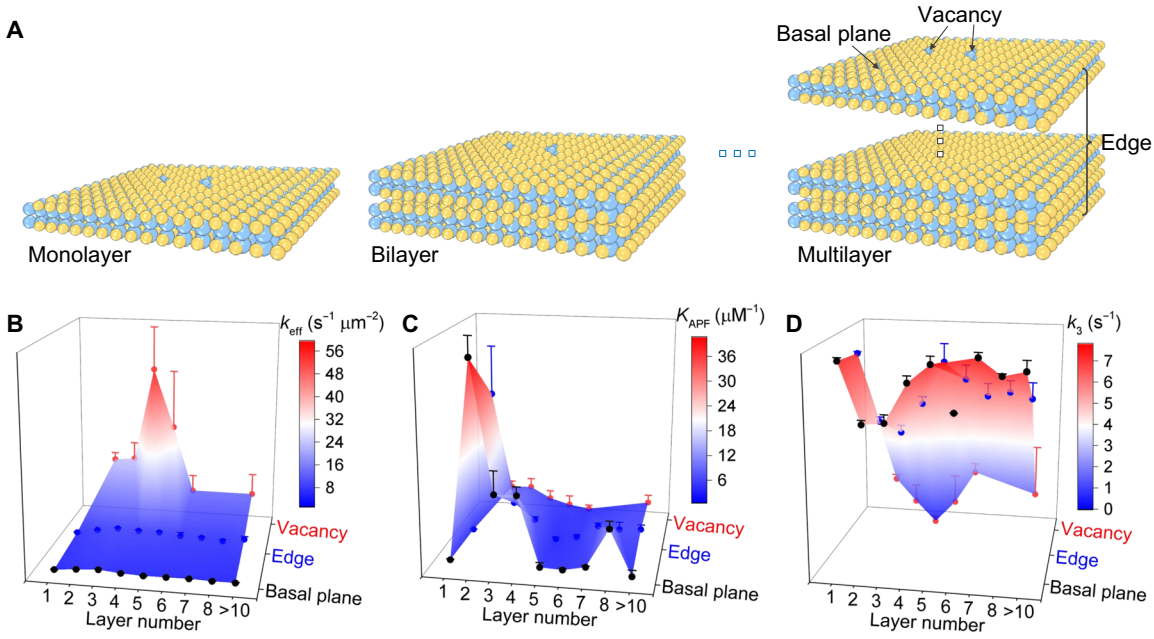

Fig. 3. Layer-dependent photocatalytic kinetics at different structural features of 2D layered InSe. (**A**) Schematic of basal plane, edge, and vacancy in InSe flakes with different layer thicknesses. (**B**) Reaction rate constant k_{eff}. (**C**) Adsorption equilibrium constant of APF, K_{APF}. (**D**) Dissociation rate constants of fluorescein, k_3. The error bars are the SDs in Gaussian fitting the distribution of kinetic parameters from many subregions (basal plane > 1000, edge > 300, and vacancy > 50) over more than 40 InSe flakes.

bandgap semiconductor have longer lifetimes and diffusion lengths (*39*), so they can be used for the catalytic reaction with higher probabilities. Therefore, photocatalytic activity would increase as layer thickness decreases because of the transition of the bandgap structure from direct to indirect. Second, the photon absorption efficiency decreases with lower layer number (*33*, *45*). As a result, the photogeneration efficiency of electrons and holes decreases as InSe gets thinner, thus reducing the photocatalytic activity.

Layer-dependent adsorption strength of APF and dissociation rate of fluorescein were also systematically investigated. The adsorption strength of APF is the highest on the basal plane and the lowest in the vacancy in 2D layered InSe of all layer numbers (Fig. 3C). Furthermore, the adsorption strength of APF at all structural features remains constant for thicker InSe (more than eight layers) but increases with thinner InSe (two to seven layers). A further decrease of the layer number to monolayer would lead to a marked decrease in the adsorption strength of APF as well. This is possibly due to the presence of repulsive force between the hydrophobic APF and the hydrophilic supporting quartz slide because the monolayer InSe is thinner than the penetration depth of wettability from the supporting substrate (*46*). On the other hand, higher fluorescein dissociation rate on the basal plane in comparison to that in defects was observed in all layer numbers of InSe (Fig. 3D). Nonetheless, the dependence of the fluorescein dissociation rate on layer number is less clear and seems to be the opposite trend as compared to the results from APF adsorption strength.

Surface diffusion behaviors at individual defects

One peculiar yet interesting observation that we found from the study of temporal fluctuation of reaction and dissociation rates is that catalytic reaction sites and product desorption sites in InSe are not necessarily the same (section S9 and fig. S16). Similar phenomenon has also been observed on the single-molecule imaging of metal nanoparticle catalysis (*25*, *47*). This result suggests a diffusion of fluorescein happening between the catalytic site and the desorption site. Hence, it is vital to uncover the kinematic behaviors of fluorescein molecules at different structural features. Figure 4B shows that apparent diffusion coefficients of fluorescein (the detailed calculation method is shown in section S10) at basal plane, edge, wrinkle, and vacancy are in descending order. This result suggests a gradual increase of interaction between fluorescein and these four structural features, which agrees with the results of dissociation rates shown in Fig. 2F.

To further understand the surface diffusion behaviors of fluorescein at these InSe structural features, we tracked the lateral movements of single fluorescein molecules. Figure 4A exhibits the single-molecule trajectories over InSe, showing that fluorescein diffuses on the surface for a short time until it lastly desorbed from the surface and diffuses into the bulk solution. Two distinct modes of the movement were observed, leading to three types of tracks, namely, mobile, immobile, and hybrid, as shown in Fig. 4A (inset). Details about the classification of diffusion behaviors are discussed in section S10. The fractions of three diffusion behaviors vary among different structural features (table S1). The basal plane and edge have considerable portions of mobile tracks at ~30%. However, fluorescein seems more easily trapped at the wrinkle and vacancy, resulting in a smaller population of mobile tracks (12 and 5%, respectively).

While the dissociation kinetics are significantly different at these structural features in InSe because of their intrinsic physicochemical properties (Fig. 2F), we also found that diffusion behaviors of fluorescein can also affect the dissociation rates at the same structural features. The dissociation rates of immobile tracks are smaller than that of mobile tracks in all structural features (Fig. 4C). This difference

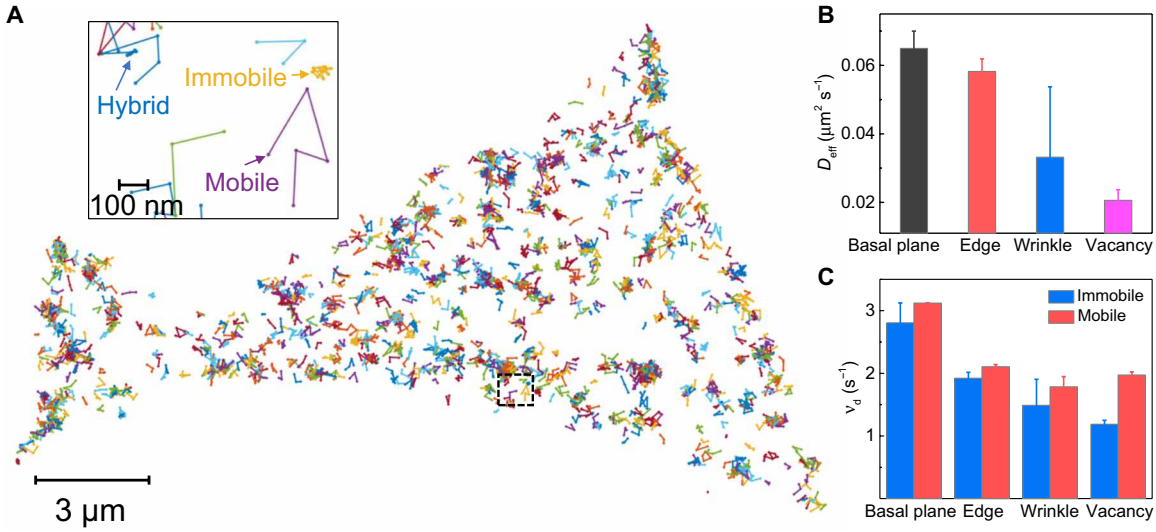

Fig. 4. Surface diffusion dynamics of fluorescein on 2D layered InSe. (**A**) Single-molecular tracks over InSe (Fig. 1) during a short imaging period under 1 μM APF in 1× phosphate-buffered saline (PBS) buffer. The interval between the two data points is 0.1 s. Inset: The zoom-in single-molecular tracks marked by the dash square in (A). Three types of tracks on InSe, showing immobile, mobile, and hybrid trajectories. (**B**) Apparent diffusion coefficients of fluorescein at different structural features under 1 μM APF in 1× PBS buffer. The error bars are means ± SD (basal plane > 250, edge > 80, wrinkle > 30, and vacancy > 10). (**C**) Dissociation rate (v_d) of direct desorption pathway and desorption-mediated diffusion pathway at different structural features derived from the traces of immobile and mobile fluorescein, respectively. The error bars were calculated as the uncertainty of Gaussian fitting the distribution of dissociation rates from immobile and mobile tracks (Immobile tracks: basal plane, ~100; edge, ~48; wrinkle, ~72; and vacancy, ~290; mobile tracks: basal plane, ~131; edge, ~143; wrinkle, ~54; and vacancy, ~47).

results from their different desorption mechanisms. For the immobile molecule, it needs to overcome the large energy barrier for direct desorption (fig. S18). In contrast, the mobile behaviors of molecules on the surface have been attributed to desorption-mediated diffusion (*48*–*51*). In this mechanism, the molecule desorbs from the surface, diffuses in the adjacent liquid phase, and readsorbs at a new location on the surface before it completely desorbs from the surface (*48*–*51*). The activation energy of dissociation through the desorption-mediated diffusion pathway, which is associated with the corrugation of the surface interaction potential, is much smaller than the direct desorption pathway (fig. S18) (*52*). The required activation energy through these two desorption mechanisms accounts for the different dissociation rates of immobile and mobile fluorescein molecules (Fig. 4C), although they are located at the same structural features.

DISCUSSION

We have spatially resolved the heterogeneous dynamics of photocatalytic processes at individual defects in 2D layered InSe using single-molecule fluorescence imaging with high spatial and temporal resolution. From the localization mapping results, we visualized and distinguished the photocatalytic activity at individual structural features on 2D layered InSe. We found that the highest catalytic active InSe catalysts can be obtained by using the four-layer InSe as the supported pristine material and introducing vacancies for the defect engineering. We quantitatively measured the kinetic parameters of photocatalysis at individual defects. Vacancies, wrinkles, and edges show up to ~30×, ~6×, and ~4× higher photocatalytic reaction rate constant but up to ~7×, ~3×, and ~3× lower absorption strength and ~26×, ~2.2×, and ~1.8× slower dissociation rate constants when compared with the basal plane, respectively. These distinct reaction kinetic properties are determined by the intrinsic lattice structures/electronic energy levels of defects and the layer thickness of supported InSe. We further studied the surface diffusion behaviors of product, where three types of molecular diffusion behaviors (i.e., mobile, immobile, and hybrid trajectories) were observed at all defects. However, slower molecular diffusion rates were found at more photocatalytic active defects because of smaller population of mobile trajectory and stronger interaction with the product molecule. Our findings shed light on the fundamental understanding of catalytic dynamics at individual defects, which provide guidance for the rational design of high-performance 2D material catalysts via defect engineering. This work can be extended to investigate the catalytic dynamics at other defects (substitution, adatom, grain boundary, etc.) and defects in other 2D layered materials. Continued efforts on establishing the molecular level understanding of how the defect chemical modification and external modulations (e.g., electric control, magnetic field, and supporting matrix effects) affect the catalytic dynamics at defects are worthy of future devotion.

MATERIALS AND METHODS

Sample preparation

Bulk InSe crystal was fabricated by using a nonstoichiometric melt of indium and selenium (*53*). InSe layered samples were obtained by mechanical exfoliation (*54*, *55*). In brief, freshly cleaved InSe was fabricated on Scotch tape and then repeatedly peeled off to produce plenty of thin InSe flakes. We stamp-transferred the flakes onto the clean quartz slide (fused, 76.2 mm by 25.4 mm by 1.0 mm, Alfa Aesar) while heating the substrate to 65°C. Afterward, the quartz slide–supported InSe flakes were annealed under a nitrogen atmosphere at 65°C for 30 min and lastly inspected under an optical microscope to select the interested InSe flakes.

Single-molecule fluorescence imaging

Single-molecule imaging experiments were carried on a prism-type total internal reflection fluorescence microscope (*14*, *15*) with setup configurations including an adjustable 60 mW/488 nm continuous wave laser (Oxxius), a 60× water immersion objective (Olympus; NA, 1.2), an iXonEM$^+$ Ultra 897 camera (Andor Technology; 512 × 512 imaging array; 16 μm by 16 μm pixel size), and a fluorescence filter set composed of a Chroma quad cube (ET-405/488/561/640-nm Laser Quad Band) and a 535/50-nm band-pass filter (Semrock). The exposure time of each frame is 100 ms. The photocatalytic activity of InSe samples was measured by using a fluorogenic reaction of nonfluorescent APF (Thermo Fisher Scientific) chemoselectively reacting with hydroxyl radicals to produce highly fluorescent fluorescein (maximum excitation wavelength, λ_{ex} = 490 nm and maximum emission wavelength, λ_{em} = 512 nm at pH 7.4). A microflow chamber was prepared by assembling the quartz slide with InSe sample and a #1.5 coverslip using 120-μm-thick double-side tape. A reaction solution composed of APF and 1× phosphate-buffered saline buffer (pH 7.4) was introduced into the microflow chamber using a syringe pump (Harvard) with a flow rate set to 20 μl min^{-1}.

SUPPLEMENTARY MATERIALS

Supplementary material for this article is available at https://science.org/doi/10.1126/sciadv.abj4452

REFERENCES AND NOTES

1. H. Zhang, R. Lv, Defect engineering of two-dimensional materials for efficient electrocatalysis. *J. Materiomics* **4**, 95–107 (2018).
2. X. Chia, M. Pumera, Characteristics and performance of two-dimensional materials for electrocatalysis. *Nat. Catal.* **1**, 909–921 (2018).
3. T. F. Jaramillo, K. P. Jorgensen, J. Bonde, J. H. Nielsen, S. Horch, I. Chorkendorff, Identification of active edge sites for electrochemical H_2 evolution from MoS_2 nanocatalysts. *Science* **317**, 100–102 (2007).
4. Z. Lin, B. R. Carvalho, E. Kahn, R. Lv, R. Rao, H. Terrones, M. A. Pimenta, M. Terrones, Defect engineering of two-dimensional transition metal dichalcogenides. *2D Mater.* **3**, 022002 (2016).
5. Z. Wu, Z. Ni, Spectroscopic investigation of defects in two-dimensional materials. *Nanophotonics* **6**, 1219–1237 (2017).
6. W. Zhou, X. Zou, S. Najmaei, Z. Liu, Y. Shi, J. Kong, J. Lou, P. M. Ajayan, B. I. Yakobson, J.-C. Idrobo, Intrinsic structural defects in monolayer molybdenum disulfide. *Nano Lett.* **13**, 2615–2622 (2013).
7. Y. L. Huang, Y. Chen, W. Zhang, S. Y. Quek, C.-H. Chen, L.-J. Li, W.-T. Hsu, W.-H. Chang, Y. J. Zheng, W. Chen, A. T. S. Wee, Bandgap tunability at single-layer molybdenum disulphide grain boundaries. *Nat. Commun.* **6**, 6298 (2015).
8. T.-X. Huang, X. Cong, S.-S. Wu, K.-Q. Lin, X. Yao, Y.-H. He, J.-B. Wu, Y.-F. Bao, S.-C. Huang, X. Wang, P.-H. Tan, B. Ren, Probing the edge-related properties of atomically thin MoS_2 at nanoscale. *Nat. Commun.* **10**, 5544 (2019).
9. Y. Luo, R. Engelke, M. Mattheakis, M. Tamagnone, S. Carr, K. Watanabe, T. Taniguchi, E. Kaxiras, P. Kim, W. L. Wilson, In situ nanoscale imaging of moiré superlattices in twisted van der Waals heterostructures. *Nat. Commun.* **11**, 4209 (2020).
10. D. Deng, K. S. Novoselov, Q. Fu, N. Zheng, Z. Tian, X. Bao, Catalysis with two-dimensional materials and their heterostructures. *Nat. Nanotechnol.* **11**, 218–230 (2016).
11. X. Zhou, N. M. Andoy, G. Liu, E. Choudhary, K.-S. Han, H. Shen, P. Chen, Quantitative super-resolution imaging uncovers reactivity patterns on single nanocatalysts. *Nat. Nanotechnol.* **7**, 237–241 (2012).
12. K. Naito, T. Tachikawa, M. Fujitsuka, T. Majima, Single-molecule observation of photocatalytic reaction in TiO_2 nanotube: Importance of molecular transport through porous structures. *J. Am. Chem. Soc.* **131**, 934–936 (2009).
13. M. B. J. Roeffaers, B. F. Sels, H. Uji-i, F. C. De Schryver, P. A. Jacobs, D. E. De Vos, J. Hofkens, Spatially resolved observation of crystal-face-dependent catalysis by single turnover counting. *Nature* **439**, 572–575 (2006).
14. B. Dong, Y. Pei, N. Mansour, X. Lu, K. Yang, W. Huang, N. Fang, Deciphering nanoconfinement effects on molecular orientation and reaction intermediate by single molecule imaging. *Nat. Commun.* **10**, 4815 (2019).
15. B. Dong, Y. Pei, F. Zhao, T. W. Goh, Z. Qi, C. Xiao, K. Chen, W. Huang, N. Fang, In situ quantitative single-molecule study of dynamic catalytic processes in nanoconfinement. *Nat. Catal.* **1**, 135–140 (2018).
16. B. Dong, N. Mansour, Y. Pei, Z. Wang, T. Huang, S. L. Filbrun, M. Chen, X. Cheng, M. Pruski, W. Huang, N. Fang, Single molecule investigation of nanoconfinement hydrophobicity in heterogeneous catalysis. *J. Am. Chem. Soc.* **142**, 13305–13309 (2020).
17. T. Tachikawa, S. Yamashita, T. Majima, Probing photocatalytic active sites on a single titanosilicate zeolite with a redox-responsive fluorescent dye. *Angew. Chem. Int. Ed.* **49**, 432–435 (2010).
18. T. Tachikawa, P. Zhang, Z. Bian, T. Majima, Efficient charge separation and photooxidation on cobalt phosphate-loaded TiO_2 mesocrystal superstructures. *J. Mater. Chem. A* **2**, 3381–3388 (2014).
19. P. Vancsó, G. Z. Magda, J. Pető, J.-Y. Noh, Y.-S. Kim, C. Hwang, L. P. Biró, L. Tapasztó, The intrinsic defect structure of exfoliated MoS_2 single layers revealed by scanning tunneling microscopy. *Sci. Rep.* **6**, 29726 (2016).
20. J. Pető, T. Ollár, P. Vancsó, Z. I. Popov, G. Z. Magda, G. Dobrik, C. Hwang, P. B. Sorokin, L. Tapasztó, Spontaneous doping of the basal plane of MoS_2 single layers through oxygen substitution under ambient conditions. *Nat. Chem.* **10**, 1246–1251 (2018).
21. H. Li, C. Tsai, A. L. Koh, L. Cai, A. W. Contryman, A. H. Fragapane, J. Zhao, H. S. Han, H. C. Manoharan, F. Abild-Pedersen, J. K. Norskov, X. Zheng, Activating and optimizing MoS_2 basal planes for hydrogen evolution through the formation of strained sulphur vacancies. *Nat. Mater.* **15**, 48–53 (2016).
22. D. Axelrod, Total internal reflection fluorescence microscopy, in *Methods in Cell Biology*, L. Wilson, P. Matsudaira, Eds. (Elsevier, 2008), vol. 89, pp. 169–221.
23. L. Song, R. P. M. van Gijlswijk, I. T. Young, H. J. Tanke, Influence of fluorochrome labeling density on the photobleaching kinetics of fluorescein in microscopy. *Cytometry* **27**, 213–223 (1997).
24. L. Song, E. Hennink, I. T. Young, H. J. Tanke, Photobleaching kinetics of fluorescein in quantitative fluorescence microscopy. *Biophys. J.* **68**, 2588–2600 (1995).
25. W. Xu, J. S. Kong, Y.-T. E. Yeh, P. Chen, Single-molecule nanocatalysis reveals heterogeneous reaction pathways and catalytic dynamics. *Nat. Mater.* **7**, 992–996 (2008).
26. W. Xu, J. S. Kong, P. Chen, Single-molecule kinetic theory of heterogeneous and enzyme catalysis. *J. Phys. Chem. C* **113**, 2393–2404 (2009).
27. W. Xu, H. Shen, G. Liu, P. Chen, Single-molecule kinetics of nanoparticle catalysis. *Nano Res.* **2**, 911–922 (2009).
28. H. Shen, W. Xu, P. Chen, Single-molecule nanoscale electrocatalysis. *Phys. Chem. Chem. Phys.* **12**, 6555–6563 (2010).
29. K. S. Han, G. Liu, X. Zhou, R. E. Medina, P. Chen, How does a single Pt nanocatalyst behave in two different reactions? A single-molecule study. *Nano Lett.* **12**, 1253–1259 (2012).
30. D. J. Trainer, Y. Zhang, F. Bobba, X. Xi, S.-W. Hla, M. Iavarone, The effects of atomic-scale strain relaxation on the electronic properties of monolayer MoS_2. *ACS Nano* **13**, 8284–8291 (2019).
31. H. Yang, P. Zhao, Y. Ma, X. Lv, B. Huang, Y. Dai, Janus single-layer group-III monochalcogenides: A promising visible-light photocatalyst. *J. Phys. D Appl. Phys.* **52**, 455303 (2019).
32. B. Wang, H. Yuan, J. Chang, X. Chen, H. Chen, Two dimensional InSe/C_2N van der Waals heterojunction as enhanced visible-light-responsible photocatalyst for water splitting. *Appl. Surf. Sci.* **485**, 375–380 (2019).
33. M. Wu, J.-j. Shi, M. Zhang, Y.-m. Ding, H. Wang, Y.-l. Cen, J. Lu, Enhancement of photoluminescence and hole mobility in 1- to 5-layer InSe due to the top valence-band inversion: Strain effect. *Nanoscale* **10**, 11441–11451 (2018).
34. Y. Liang, C. Long, J. Li, H. Jin, B. Huang, Y. Dai, InSe monolayer: Promising cocatalyst of g-C_3N_4 for water splitting under visible light. *ACS Appl. Energy Mater.* **1**, 5394–5401 (2018).
35. K. J. Xiao, A. Carvalho, A. H. Castro Neto, Defects and oxidation resilience in InSe. *Phys. Rev. B* **96**, 054112 (2017).
36. C.-H. Ho, C.-H. Lin, Y.-P. Wang, Y.-C. Chen, S.-H. Chen, Y.-S. Huang, Surface oxide effect on optical sensing and photoelectric conversion of α-In_2Se_3 hexagonal microplates. *ACS Appl. Mater. Interfaces* **5**, 2269–2277 (2013).
37. A. A. Kistanov, Y. Cai, K. Zhou, S. V. Dmitriev, Y.-W. Zhang, Atomic-scale mechanisms of defect- and light-induced oxidation and degradation of InSe. *J. Mater. Chem. C* **6**, 518–525 (2018).
38. X. Wei, C. Dong, A. Xu, X. Li, D. D. Macdonald, Oxygen-induced degradation of the electronic properties of thin-layer InSe. *Phys. Chem. Chem. Phys.* **20**, 2238–2250 (2018).
39. J. Zhang, P. Zhou, J. Liu, J. Yu, New understanding of the difference of photocatalytic activity among anatase, rutile and brookite TiO_2. *Phys. Chem. Chem. Phys.* **16**, 20382–20386 (2014).
40. O. H. Pakarinen, J. M. Mativetsky, A. Gulans, M. J. Puska, A. S. Foster, P. Grutter, Role of van der Waals forces in the adsorption and diffusion of organic molecules on an insulating surface. *Phys. Rev. B* **80**, 085401 (2009).
41. M. Pandey, K. S. Thygesen, Two-dimensional MXenes as catalysts for electrochemical hydrogen evolution: A computational screening study. *J. Phys. Chem. C* **121**, 13593–13598 (2017).

42. J. Shang, L. Pan, X. Wang, J. Li, Z. Wei, Tunable electric properties of bilayer InSe with different interlayer distances and external electric field. *Semicond. Sci. Tech.* **33**, 034002 (2018).
43. M. J. Hamer, J. Zultak, A. V. Tyurnina, V. Zólyomi, D. Terry, A. Barinov, A. Garner, J. Donoghue, A. P. Rooney, V. Kandyba, A. Giampietri, A. Graham, N. Teutsch, X. Xia, M. Koperski, S. J. Haigh, V. I. Fal'ko, R. V. Gorbachev, N. R. Wilson, Indirect to direct gap crossover in two-dimensional InSe revealed by angle-resolved photoemission spectroscopy. *ACS Nano* **13**, 2136–2142 (2019).
44. G. W. Mudd, M. R. Molas, X. Chen, V. Zólyomi, K. Nogajewski, Z. R. Kudrynskyi, Z. D. Kovalyuk, G. Yusa, O. Makarovsky, L. Eaves, M. Potemski, V. I. Fal'ko, A. Patanè, The direct-to-indirect band gap crossover in two-dimensional van der Waals Indium Selenide crystals. *Sci. Rep.* **6**, 39619 (2016).
45. M. Brotons-Gisbert, D. Andres-Penares, J. Suh, F. Hidalgo, R. Abargues, P. J. Rodríguez-Cantó, A. Segura, A. Cros, G. Tobias, E. Canadell, P. Ordejón, J. Wu, J. P. Martínez-Pastor, J. F. Sánchez-Royo, Nanotexturing to enhance photoluminescent response of atomically thin Indium Selenide with highly tunable band Gap. *Nano Lett.* **16**, 3221–3229 (2016).
46. T. Tian, C.-J. Shih, Molecular epitaxy on two-dimensional materials: The interplay between interactions. *Ind. Eng. Chem. Res.* **56**, 10552–10581 (2017).
47. W. Xu, J. S. Kong, P. Chen, Probing the catalytic activity and heterogeneity of Au-nanoparticles at the single-molecule level. *Phys. Chem. Chem. Phys.* **11**, 2767–2778 (2009).
48. M. J. Skaug, J. N. Mabry, D. K. Schwartz, Single-molecule tracking of polymer surface diffusion. *J. Am. Chem. Soc.* **136**, 1327–1332 (2014).
49. M. J. Skaug, A. M. Lacasta, L. Ramirez-Piscina, J. M. Sancho, K. Lindenberg, D. K. Schwartz, Single-molecule diffusion in a periodic potential at a solid–liquid interface. *Soft Matter* **10**, 753–759 (2014).
50. M. J. Skaug, J. Mabry, D. K. Schwartz, Intermittent molecular hopping at the solid-liquid interface. *Phys. Rev. Lett.* **110**, 256101 (2013).
51. R. Walder, N. Nelson, D. K. Schwartz, Single molecule observations of desorption-mediated diffusion at the solid-liquid interface. *Phys. Rev. Lett.* **107**, 156102 (2011).
52. B. B. Langdon, M. Kastantin, D. K. Schwartz, Apparent activation energies associated with protein dynamics on hydrophobic and hydrophilic surfaces. *Biophys. J.* **102**, 2625–2633 (2012).
53. S. Lei, L. Ge, S. Najmaei, A. George, R. Kappera, J. Lou, M. Chhowalla, H. Yamaguchi, G. Gupta, R. Vajtai, A. D. Mohite, P. M. Ajayan, Evolution of the electronic band structure and efficient photo-detection in atomic layers of InSe. *ACS Nano* **8**, 1263–1272 (2014).
54. K. S. Novoselov, A. K. Geim, S. V. Morozov, D. Jiang, M. I. Katsnelson, I. V. Grigorieva, S. V. Dubonos, A. A. Firsov, Two-dimensional gas of massless Dirac fermions in graphene. *Nature* **438**, 197–200 (2005).
55. A. Castellanos-Gomez, M. Buscema, R. Molenaar, V. Singh, L. Janssen, D. Z. Van, S. J. Herre, G. A. Steele, Deterministic transfer of two-dimensional materials by all-dry viscoelastic stamping. *2D Mater.* **1**, 011002 (2013).
56. K.-i. Setsukinai, Y. Urano, K. Kakinuma, H. J. Majima, T. Nagano, Development of novel fluorescence probes that can reliably detect reactive oxygen species and distinguish specific species. *J. Biol. Chem.* **278**, 3170–3175 (2003).
57. R. E. Thompson, D. R. Larson, W. W. Webb, Precise nanometer localization analysis for individual fluorescent probes. *Biophys. J.* **82**, 2775–2783 (2002).
58. A. Castellanos-Gomez, R. Roldán, E. Cappelluti, M. Buscema, F. Guinea, H. S. J. van der Zant, G. A. Steele, Local strain engineering in atomically thin MoS_2. *Nano Lett.* **13**, 5361–5366 (2013).
59. A. Politano, G. Chiarello, R. Samnakay, G. Liu, B. Gürbulak, S. Duman, A. A. Balandin, D. W. Boukhvalov, The influence of chemical reactivity of surface defects on ambient-stable InSe-based nanodevices. *Nanoscale* **8**, 8474–8479 (2016).
60. P. Lazar, M. Otyepka, Role of the edge properties in the hydrogen evolution reaction on MoS_2. *Chem. A Eur. J.* **23**, 4863–4869 (2017).

Acknowledgments

Funding: This work was supported by funds from Georgia State University. N.F. also acknowledges the support from Science and Technology Projects of Innovation Laboratory for Sciences and Technologies of Energy Materials of Fujian Province (IKKEM) (RD2020050501).

Author contributions: T.-X.H., B.D., S.L., and N.F. conceived the idea, designed the experiments, and wrote the manuscript. T.-X.H. and B.D. performed the imaging experiments and data analysis. S.L. and A.A.O. performed the synthesis of InSe. S.L.F., X.C., M.Y., and N.M. helped with the data analysis and discussion. **Competing interests:** The authors declare that they have no competing interests. **Data and materials availability:** All data needed to evaluate the conclusions in the paper are present in the paper and/or the Supplementary Materials.

Submitted 14 May 2021
Accepted 10 August 2021
Published 1 October 2021
10.1126/sciadv.abj4452

Citation: T.-X. Huang, B. Dong, S. L. Filbrun, A. A. Okmi, X. Cheng, M. Yang, N. Mansour, S. Lei, N. Fang, Single-molecule photocatalytic dynamics at individual defects in two-dimensional layered materials. *Sci. Adv.* **7**, eabj4452 (2021).